AGU PUBLICATIONS

JGR

Journal of Geophysical Research: Solid Earth

RESEARCH ARTICLE
10.1002/2016JB013213

Special Section:
Stress at Active Plate Boundaries - Measurement and Analysis, and Implications for Seismic Hazard

Key Points:
- Average crustal b values are calculated within a geothermal field and next to a drilled melt pocket
- Most events in the geothermal field are consistent with double-couple mechanisms with only few non-shear-faulting events
- Normal faulting prevails in the central caldera with the least compressive stress closely aligned with the plate spreading direction

Correspondence to:
J. Schuler,
schuler@cantab.net

Citation:
Schuler, J., D. J. Pugh, E. Hauksson, R. S. White, J. M. Stock, and B. Brandsdóttir (2016), Focal mechanisms and size distribution of earthquakes beneath the Krafla central volcano, NE Iceland, *J. Geophys. Res. Solid Earth*, *121*, 5152–5168, doi:10.1002/2016JB013213.

Received 26 MAY 2016
Accepted 12 JUL 2016
Accepted article online 18 JUL 2016
Published online 28 JUL 2016

Focal mechanisms and size distribution of earthquakes beneath the Krafla central volcano, NE Iceland

Juerg Schuler[1], David J. Pugh[2,3], Egill Hauksson[1], Robert S. White[2], Joann M. Stock[1], and Bryndís Brandsdóttir[4]

[1]Seismological Laboratory California Institute of Technology, Pasadena, California, USA, [2]Bullard Laboratories, University of Cambridge, Cambridge, UK, [3]Now at McLaren Applied Technologies, Woking, UK, [4]Science Institute, University of Iceland, Reykjavík, Iceland

Abstract Seismicity was monitored beneath the Krafla central volcano, NE Iceland, between 2009 and 2012 during a period of volcanic quiescence, when most earthquakes occurred within the shallow geothermal field. The highest concentration of earthquakes is located close to the rock-melt transition zone as the Iceland Deep Drilling Project-1 (IDDP-1) wellbore suggests and decays quickly at greater depths. We recorded multiple swarms of microearthquakes, which coincide often with periods of changes in geothermal field operations, and found that about one third of the total number of earthquakes are repeating events. The event size distribution, evaluated within the central caldera, indicates average crustal values with $b = 0.79 \pm 0.04$. No significant spatial b value contrasts are resolved within the geothermal field nor in the vicinity of the drilled melt. Besides the seismicity analysis, focal mechanisms are calculated for 342 events. Most of these short-period events have source radiation patterns consistent with double-couple (DC) mechanisms. A few events are attributed to non-shear-faulting mechanisms with geothermal fluids likely playing an important role in their source processes. Diverse faulting styles are inferred from DC events, but normal faulting prevails in the central caldera. The best fitting compressional and tensional axes of DC mechanisms are interpreted in terms of the principal stress or deformation rate orientations across the plate boundary rift. Maximum compressive stress directions are near-vertically aligned in different study volumes, as expected in an extensional tectonic setting. Beneath the natural geothermal fields, the least compressive stress axis is found to align with the regional spreading direction. In the main geothermal field both horizontal stresses appear to have similar magnitudes causing a diversity of focal mechanisms.

1. Introduction

The Mid-Atlantic Ridge, crossing Iceland, is expressed by en échelon-arranged volcanic systems that commonly include a central volcano and fissure swarm [*Sæmundsson*, 1979]. Our focus is the Krafla volcanic system in NE Iceland (Figure 1) comprising a 5–8 km wide and 100 km long fissure swarm trending approximately N10°E and transecting its 21 km by 17 km wide central volcano and caldera [*Hjartardóttir et al.*, 2012]. Its volcano, estimated to be 0.5–1.8 Myr old [*Brandsdóttir et al.*, 1997], underwent 35 eruptions since the last glacial period [*Björnsson et al.*, 1979]. The *Krafla fires* is the last rifting episode and occurred between 1974 and 1984. It included 20 rifting events and nine basaltic fissure eruptions [*Einarsson*, 1991; *Buck et al.*, 2006].

Based on the wave propagation path of regional earthquakes, *Brandsdóttir and Einarsson* [1979] inferred that magma was stored in shallow chambers and sporadically injected into dikes along the fissure swarm. Seismicity ceased after the rifting episode and has been mostly confined to two high-temperature geothermal systems [e.g., *Arnott and Foulger*, 1994a; *Schuler et al.*, 2015], where faults and fissures facilitate the transfer of hot geothermal fluids to the surface. The Bjarnarflag-Námafjall field is located outside whereas the Krafla-Leirhnjúkur field is located inside the caldera. Geothermal drilling started in 1974 and energy production started in 1977. Drill cuttings from boreholes helped to construct local geological profiles of the eastern and southeastern caldera [*Ármansson et al.*, 1987]. At Hvíthólar (Figure 1b), lavas and hyaloclastites dominate the upper 1.5–1.6 km of the rock sequence followed by intrusive rocks (gabbro). In the Leirbotnar-Suðurhlíðar area, lavas and hyaloclastites are encountered to 1.0 km depth or 0.5 km below sea level (bsl) overlying gabbroic rocks, whereas to the east of Suðurhlíðar, gabbroic intrusive rocks are found at 1.2–1.3 km bsl (from here onward, we refer to depth as depth below the surface if not followed by the acronym bsl).

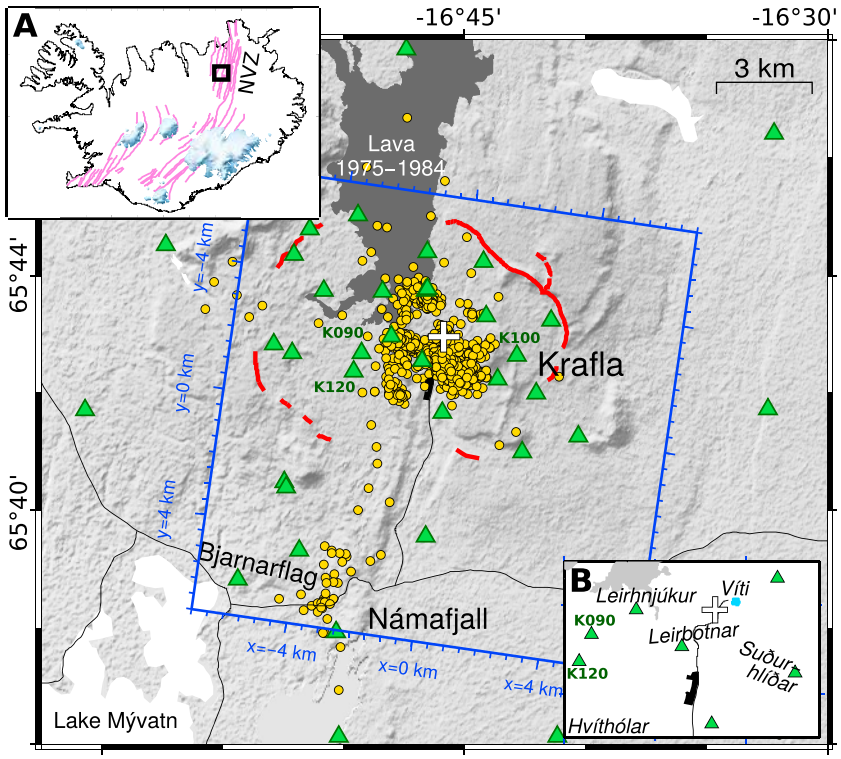

Figure 1. Map of the study area. Station locations are marked by green triangles, the mapped caldera rim in red, the IDDP-1 well as white cross, and manually picked earthquakes with yellow circles. Our local analysis grid is colored in blue, and lava flows of the Krafla fires are shaded in dark grey. (a) Map of Iceland, the location of the Krafla volcano (box) in the Northern Volcanic Zone (NVZ), and the fissures of the volcanic systems (purple lines) delineating the plate boundary. (b) An enlarged map of the central caldera.

While drilling the Iceland Deep Drilling Project-1 (IDDP-1) borehole in 2009, rhyolitic melt was encountered at 2104 m depth (1551 m bsl). Its location is 0.5 km southwest of the 1724 AD explosion crater Víti. The melt likely originated from partially molten and hydrothermally altered crust [*Elders et al.*, 2011; *Zierenberg et al.*, 2012]. Above the melt pocket at 1482–1527 m depth bsl, the most productive zone for fluid injections was located in felsic rock [*Mortensen et al.*, 2014; *Friðleifsson et al.*, 2015]. Another well, KJ-39, retrieved quenched silicic glass southeast of IDDP-1 at 2062 m depth bsl [*Mortensen et al.*, 2010], but chemical differences indicate no direct link between the melt sources.

Rhyolitic domes and ridges near the caldera rim suggest that magma chambers existed in the past beneath the volcano, because these rhyolites were likely generated at the sides of an active magma chamber [*Jónasson*, 2007]. Whether the drilled melt in IDDP-1 is part of a large magma chamber has not been fully determined. Seismic studies [e.g., *Einarsson*, 1978; *Brandsdóttir and Menke*, 1992; *Schuler et al.*, 2015] as well as joint magnetotelluric and transient electromagnetic soundings [e.g., *Árnason et al.*, 2009] point toward the presence of a larger heat source emanating from multiple shallow dikes, a larger melt pocket cooling at shallow depth, and/or heat being supplied from a depth farther below.

Seismic data were acquired initially to image the shallow magma chamber [*Schuler et al.*, 2015]. Here we investigate the earthquake seismicity and source mechanisms close to the melt-rock interface and in the overlying geothermal field to better understand the processes involved. In addition, we examine the crustal stress state or deformation rate at Krafla a quarter century after the last rifting episode.

2. Data

A seismic array comprising 27 Güralp 6TD/30s and one ESPCD/60s instruments, complemented by 4 LE-3D/5s stations that were operated by the Icelandic Meteorological Office (IMO), collected data during the period from August 2009 to July 2012. Station distributions changed slightly over time, which entails that we study and compare only consistent subsets of data without testing the effect of a network change. Typically,

25 seismometers were recording earthquakes down to local magnitudes (ML) of about −1. Noise levels appear to be fairly constant at each receiver over different time periods. We used the Coalescence Microseismic Mapping (CMM) method by *Drew et al.* [2013] for initial detection and localization of earthquakes. Arrival-time picks of events with high signal-to-noise ratio (SNR) were manually refined. Hypocenter locations were taken from *Schuler et al.* [2015], who determined them by a 3-D tomographic inversion. Improved relative locations (Figure 1) are achieved by double-difference calculations [*Waldhauser and Ellsworth*, 2000] using the 3-D velocity model. Hypocenter location errors, estimated during the tomographic inversion, are mostly less than 150 m. The peak frequencies of *P* wave first arrivals are typically about 10 ± 2 Hz in the central part of the caldera.

3. *b* Values in Volcanic Areas

The size distribution of earthquakes within a seismogenic volume and time period is commonly described by the power law [*Ishimoto and Iida*, 1939; *Gutenberg and Richter*, 1944] $\log N = a - bM$, with N being the cumulative earthquake number of events with magnitudes $\geq M$, a being the productivity of the considered volume, and b is the relative size distribution. Some factors affecting the b value are material heterogeneity [*Mogi*, 1962], thermal gradient [*Warren and Latham*, 1970], and applied stress [*Scholz*, 1968; *Schorlemmer et al.*, 2005]. For tectonic regions, b averages to about 1.0 [*Frohlich and Davis*, 1993]. In volcanic areas, high b values ($b \geq 1.3$) are mostly resolved in small volumes embedded in average ($b \leq 1.0$) crust [e.g., *Wiemer and McNutt*, 1997]. In particular, elevated b values are found close to magma chambers, where strong heterogeneities, thermal gradients, high pore pressures, extensive fracture systems, and circulating geothermal fluids are expected [*Wiemer and Wyss*, 2002]. Volcanic zones that exhibit elevated b values, collocated with inferred magma pockets, have been reported for both deeper (7–10 km) and shallower (3–4 km) depths [*McNutt*, 2005]. *McNutt* [2005] recognized that there is often a characteristic temporal b value sequence associated with volcanic intrusions and eruptions. The first short-term b value peak is attributed to high geothermal gradients [*Warren and Latham*, 1970], whereas a following longer-lived b value peak is caused by an increase of the pore pressure analogous to a reservoir undergoing fluid injections [*Wyss*, 1973]. Thereafter, b values return to normal crustal levels.

At the Krafla volcano, *Ward et al.* [1969] estimated a $b = 0.84 \pm 0.29$ and $b = 0.83 \pm 0.16$ using *P* and *S* wave amplitudes, respectively, in the central part of the caldera prior to the Krafla fires in 1967. During the rifting episode in 1978, *Einarsson and Brandsdóttir* [1980] obtained a high b value of 1.7 ± 0.2 for an earthquake swarm recorded during a dike injection north of Leirhnjúkur. The Mid-Atlantic Ridge is another place where high b values were estimated during swarm activities [*Sykes*, 1970]. At Krafla, *Arnott and Foulger* [1994a] recorded no major swarm activity after the last eruptive rifting episode ended, with most events interpreted as main shocks. They calculated $b = 0.95 \pm 0.23$ at Leirhnjúkur, $b = 0.62 \pm 0.14$ at Bjarnarflag, $b = 1.25 \pm 0.30$ in the dike zone between Bjarnarflag and Leirhnjúkur, and $b = 0.77 \pm 0.10$ of the entire region. The elevated values in the dike zone were likely caused by shallow intrusions [*Arnott and Foulger*, 1994a]. We investigate the size distribution next to the known location of melt to see whether increased values are found.

3.1. The *b* Value Estimation

For calculating earthquake magnitudes, we employ a local magnitude determination [*Bormann et al.*, 2013] and calibrate the formula against the South Iceland Lowland (SIL) magnitudes reported by IMO. We remove the instrument responses from the waveforms and convolve the displacement data with the response of a Wood-Anderson seismograph. The maximum peak-to-peak amplitudes were automatically determined. Station corrections are applied to account for site-specific effects. A multistation approach further reduces source-specific effects (e.g., directivity). However, smaller events are recorded at fewer stations and therefore have less well-constrained magnitude estimates. Our magnitudes and errors represent the mean magnitudes and errors that are calculated from the three-component recordings at each station. Carefully determining the magnitude of completeness (M_c), the minimum magnitude at which the earthquake catalog is complete is required before b values are estimated [*Wiemer and Wyss*, 2002]. We estimated M_c using the entire-magnitude-range method described by *Woessner and Wiemer* [2005] as well as the maximum curvature method. The maximum likelihood b value [*Tinti and Mulargia*, 1987] is determined by

$$b = \frac{1}{\log(10)\Delta M} \log\left(1 + \frac{\Delta M}{\overline{M} - M_c}\right), \tag{1}$$

where $\overline{M}$ is the sampling average of the magnitudes. The bin width is constant and was determined by our average magnitude error of 0.2. In estimating the confidence limits, we follow *Shi and Bolt* [1982]. We decided to temporally map *b* values within periods of constant station distributions and spatially at discrete nodes (grid cells). We set the minimum number of events within a volume to estimate the *b* value to 100 earthquakes, double the minimum number suggested by *Schorlemmer et al.* [2014].

Earthquake swarms may bias *b* value estimation [*Farell et al.*, 2009], because it is based on a Poissonian event distribution. Related earthquakes, like foreshocks and aftershocks, are removed prior to calculating the background *b*. A cumulative rate method was employed to identify earthquake swarms using similar parameterizations to those described by *Jacobs et al.* [2013]. The minimum event number of a potential earthquake swarm was set to four above the average event rate. A distance rule is applied where earthquakes with greater distance than 10 km from the mean event location of a potential swarm are rejected. Finally, a time rule ensures that different swarm sequences are separated by at least 4 days. Whether *b* values changed significantly after removing them from the complete event catalog was evaluated following *Akaike's* [1974] Information Criterion (AIC). The AIC score of both original and declustered catalogs having the same *b* values is compared to the score where the catalogs lead to different *b* values. After *Utsu* [1992],

$$\Delta\mathrm{AIC} = -2(N_1 + N_2)\ln(N_1 + N_2) + 2N_1 \ln\left(N_1 + \frac{N_2 b_1}{b_2}\right) + 2N_2 \ln\left(N_2 + \frac{N_1 b_1}{b_1}\right) - 2. \quad (2)$$

N stands for the number of earthquakes in each group. The difference in *b* values are not considered significant if $\Delta\mathrm{AIC} < 2$ [*Utsu*, 1999].

4. Seismic Source Mechanisms

When shear slip occurs on a buried fault, shear stress is released in the form of elastic waves. The far-field properties of these waves (polarities, amplitudes) are then used in estimating the source radiation pattern or mechanism. Double-couple (DC) radiation patterns are the result of shear slip on planar faults, whereas more complex radiation patterns are summarized as non-DC resulting from nonshear faulting. Involvement of fluids, slip along curved faults and fractal faulting are some possible causes that lead to earthquakes with non-DC radiation patterns in the upper crust [*Frohlich*, 1994]. Short-period non-DC events are commonly observed within geothermal areas, such as in Iceland [*Foulger and Long*, 1984] and California [*Ross et al.*, 1999; *Foulger et al.*, 2004]. Tensile faulting was reported from a geothermal field in West Bohemia, Czech Republic [*Vavryčuk*, 2002], mixed tensile and shear faulting found at Hengill-Grensdalur [*Julian et al.*, 1998], and vertical dipole radiation patterns identified inside the Long Valley caldera [*Foulger et al.*, 2004]. More rarely, implosive earthquakes are recorded in the Námafjall field and the Krafla fires dike zone [*Arnott and Foulger*, 1994b]. Most of these studies found the non-DC and DC events interspersed in space and suggested that they are linked to geothermal fluids (circulation of fluids, phase changes, or fluid compressibilities). About 70–75% of the events at Hengill-Grensdalur in Iceland were classified as non-DC mechanisms with mostly positive volumetric (explosive) components [*Miller et al.*, 1998]. At The Geysers, about 50% have significant volumetric components [*Ross et al.*, 1999] with equal numbers being implosive and explosive. Differences between these two areas are that Hengill-Grensdalur is undeveloped and water-dominated system whereas The Geysers is a steam-dominated and heavily developed system [*Ross et al.*, 1999]. Besides short-period non-DC events, long-period earthquakes are related to fluid-solid interactions with repetitive excitations such as resonance effects of fluid-filled cracks or conduits [e.g., *Chouet*, 1996; *Maeda et al.*, 2013]. Although such signals are observed at Krafla, we do not discuss them here.

The pressure (*P*), neutral (*N*), and tension (*T*) orientations, inferred from shear-faulting events, were used to interpret the stress orientations in other parts of the North Atlantic ridge [*Klein et al.*, 1977; *Foulger*, 1988]. They suggest that the least compressive stress (σ_3) is mostly aligned with the spreading direction. The unit eigenvectors of the stress tensor are called the principal stress axes ($\vec{s}_{1,2,3}$) and distinguished from the eigenvalues, which are termed principal stress magnitudes ($\sigma_1 \geq \sigma_2 \geq \sigma_3$) with positive values meaning compression. *Arnott and Foulger* [1994b] noted a high variability in the *P* and *T* axes following the Krafla fires rifting episode suggesting that the average deviatoric stresses were small. In the dike zone, the greatest compressive stress (σ_1) was aligned with the spreading direction. This observation lets them conceptualize a stress cycle that included interrifting ($\sigma_1 \simeq \sigma_2 > \sigma_3$), immediate prerifting ($\sigma_1 \simeq \sigma_2 \simeq \sigma_3$), and immediate postrifting ($\sigma_1 \simeq \sigma_2 \gg \sigma_3$) periods. We analyze and interpret *P* and *T* axes orientations of events recorded 25 years after the last rifting episode.

4.1. Calculating Focal Mechanisms

In addition to wave polarity information, amplitude ratios can help significantly to constrain the inversion of focal mechanisms [*Ross et al.*, 1999]. We prepared the amplitudes such that the signals of the manually picked events are rotated into the ray frame to analyze compressional and shear waves separately. Incidence and azimuthal angles were obtained from 3-D ray tracing the velocity model using an eikonal solver [*Vidale*, 1988; *Hole and Zelt*, 1995]. These angles were compared to angle estimates obtained by particle motion analysis. We found that the incidence and back-azimuth angles retrieved by particle motions mostly deviated less than 16° and 9°, respectively, from the ray-based estimates. Thereafter, the velocity recordings were transformed to displacement. We followed *Boore* [2003] in compensating for path effects using the 3-D ray paths and an effective seismic quality factor of 50. Based on *Schuler et al.* [2014], we regard this value as a reasonable estimate for a sequence comprising layered basalt flows, hyaloclastites, and intrusive rocks. We manually picked the *P* wave first arrival polarities on the unfiltered data to avoid interpreting the filter imprint. The peak amplitudes of the *P*- and *S* wave first arrivals, however, were determined on traces convolved with a Butterworth response of order 2 (corner passband frequencies at 1.5 Hz and 22 Hz). The polarity orientations of the receivers were verified by teleseisms.

Rock anisotropy, strong seismic attenuation, and other lateral heterogeneities are characteristics for volcanic areas and may affect our arriving amplitudes and introduce errors into the source inversion [*Frohlich*, 1994], but they can be difficult to measure [*Pugh et al.*, 2016]. Therefore, we use amplitude ratios in the source inversion where available, as these are less sensitive to path effects. A Bayesian approach is used for moment tensor source inversion by following *Pugh et al.* [2016], which allows rigorous inclusion of both measurement and location uncertainties in the resultant probability density function (PDF). The inversion approach determines the probability distribution over the moment tensor space given the observed data. *P* wave polarities can be combined with the corrected amplitude ratios to determine the source radiation pattern. The inversion was run twice, initially constrained to the DC space and then over the full range of moment tensor solutions, allowing non-DC components to be constrained along with an estimate of whether the source can be described by a DC source or not.

4.2. Estimating Crustal Stress or Deformation Rate

The first motions recorded at seismic stations are directly linked to the displacement on the fault. The local principal strain rate axes are always 45° inclined from the shear plane regardless of the rock properties (i.e., cohesion). These define the *P* and *T* axes. They are found by calculating the best match to the first motions and amplitude ratios. The principal stress directions $\vec{s}_{1,2,3}$ may be considered aligned with the *P*, *N*, and *T* axes. This assumption introduces a stress direction uncertainty of ±15° [*Célérier*, 2008]. DC focal solutions can be used to invert for a uniform stress field, but the model requires the faults to occur on randomly oriented planes of weakness (preexisting faults) and that the material behaves isotropically and linearly. Furthermore, the focal solutions need to show enough orientation diversity with the fault slip parallel to the maximum resolved shear stress and that the movement of one fault does not influence the slip direction of others. We invert for a uniform stress field using the SATSI algorithm [*Hardebeck and Michael*, 2006] by exploiting the fact that such a stress field applied to randomly oriented faults leads to a range of DC solutions [*McKenzie*, 1969]. Strike, dip direction, and dip angles of randomly picked DC nodal planes are provided as input. Based on the nodal plane ambiguity angle of about 20°, we verified that the focal diversity is sufficient to resolve the stress orientation. The inversion result represents the best fitting orientation of the principal stress axes and the relative stress magnitude ratio $R = (\sigma_1 - \sigma_2)/(\sigma_1 - \sigma_3)$, which describes the shape of the stress ellipsoid. Another model exists contrasting the uniform stress model. It assumes that crustal stress is heterogeneous but exhibits uniform frictional strength [*Smith and Heaton*, 2006]. The evolution of such heterogeneous crustal stresses may be formed by dislocation-velocity-weakening (Heaton pulse) ruptures [*Heaton*, 1990]. As *Rivera and Kanamori* [2002] suggested, both models are end-members and the real Earth likely shows characteristics of both models.

An alternative view is that fault slip inversions reliably constrain the strain rate or, more accurately, the deformation rate. Here we mainly follow the arguments of *Twiss and Unruh* [1998]. The cumulative effect of many displacements (faults) over a larger volume can be regarded as a small continuum deformation. Inverting the *P* and *T* axes thus gives most directly information about the deformation rate, which is related to stress via the rheological properties of the rock. One of the drawbacks in both stress and deformation rate approaches is that if the medium has preferred shear plane orientations (zones of weaknesses), the inverted global,

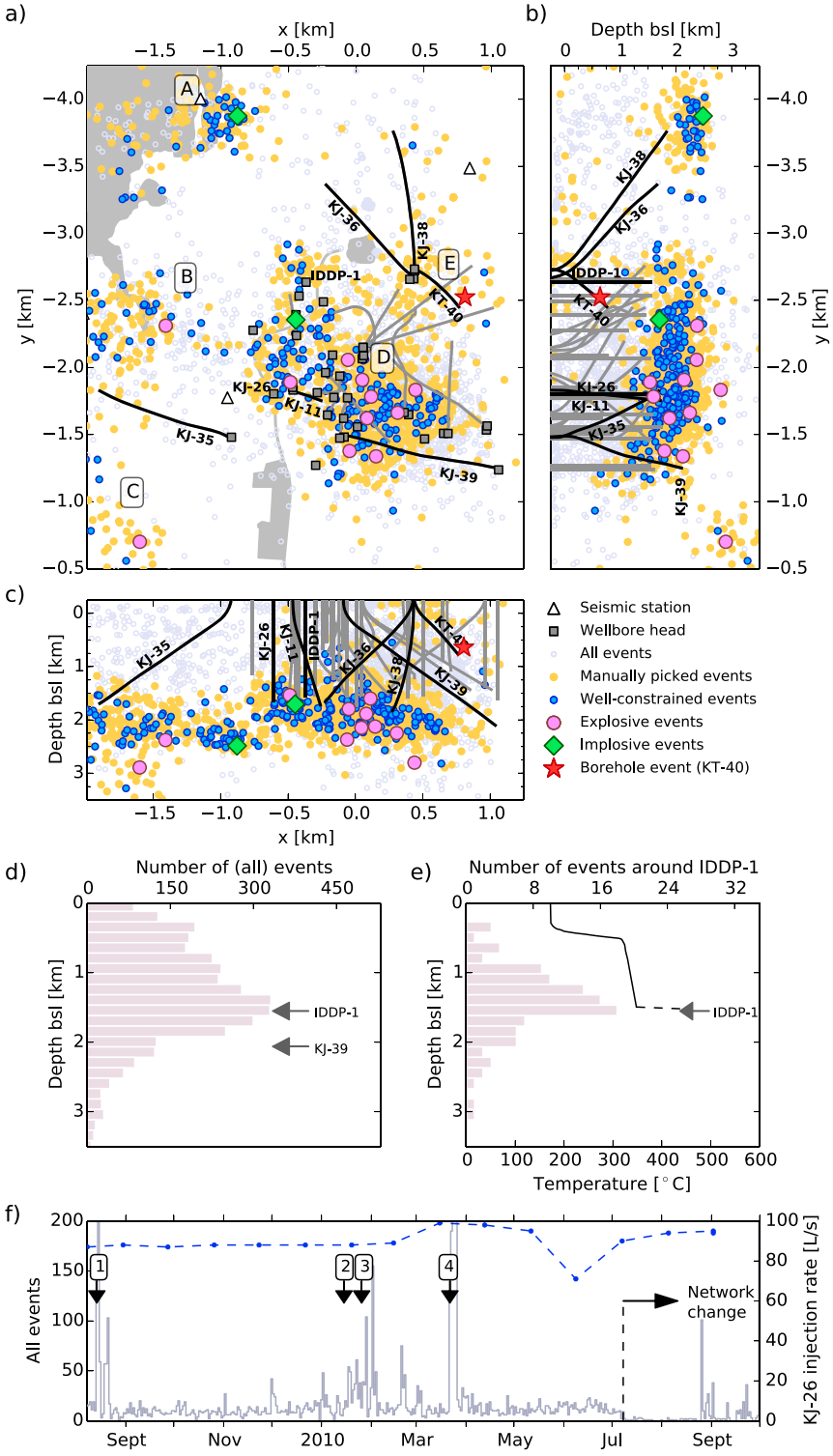

Figure 2. (a) Map of the central caldera and earthquake distribution recorded in 2009–2012. The Krafla fires lava flows, Víti crater lake, road, and power plant are shaded in dark grey. (b, c) Depth sections of the event distribution and trajectories of all wells. (d, e) Histograms illustrating the number of events versus depth. The number of events within a radius of 250 m of the IDDP-1 well are displayed in Figure 2e along with the thermal recovery profile (black line). Horizontal arrows mark the depths where melt was encountered. (f) Histograms with 1 day event bins in the area outlined in Figures 2a–2c but only for the period where we have injection volume data. Labeled arrows indicates swarms discussed in the text. The average injection rate of the main injection well KJ-26 at Krafla is superimposed (dashed blue line) after *Ágústsson et al.* [2012].

in contrast to the local, *P* and *T* axes solutions are likely to be biased, because they do not have to be perpendicular, whereas the principal stress or deformation rate axes do [*Twiss and Unruh*, 1998].

5. Results

Most of the detected seismicity is concentrated in the geothermal fields and in the uppermost 2–3 km of the crust (Figures 2a–2c). The largest number of events occur at about 1.5 km depth bsl with a relatively steep drop at greater depths (Figure 2d). Collecting events only within a radius of 250 m of the IDDP-1 borehole reveals a sharp drop of seismicity below the depth where melt was encountered (Figure 2e). A recovered thermal profile by *Friðleifsson et al.* [2015] is overlain, where superheated steam reaches about 500°C at the bottom of IDDP-1 and the melt temperature is expected to be around 900°C.

On average we detected eight events per day above magnitude −0.6 in the first 319 days and typically one to two events every day above magnitude −0.1 in the second 675 days of recording (Figure 2f). The rate change of the total number of recorded earthquakes coincides with a change in the network density. Nine periods are identified with increased seismicity rates of more than 50 additional earthquakes per day (Figure 2f). Two swarms occurred in August 2009, several larger and smaller ones in 2010, and two (not shown here) in 2011. We describe below the borehole activity preceding the four swarm periods marked in Figure 2f, but with more focus on the first one that serves as an example. Borehole activity data are compiled by *Ágústsson et al.* [2012] and *Friðleifsson et al.* [2015], as well as received by the well operator Landsvirkjun (S.H. Markússon, personal communication, 2016). Boreholes that injected relatively constant amounts of fluids are KJ-26 (0.08–0.09 m^3/s), KJ-11 (0.0085 m^3/s), KJ-38 (0.020–0.026 m^3/s), and some in KJ-35. The temperature of injected fluids is about 126°C at KJ-26/11. Preceding swarm 1 is a fluid injection stop of 0.025 m^3/s at IDDP-1 on 11 August and deepening of borehole KT-40 between 13–29 August. Events of swarm 1, located within cluster E of Figure 2a, were manually picked and relocated around KT-40. Small event magnitudes with low SNR led to large picking uncertainties. Circulation losses are reported at KT-40 and the drill bit got stuck multiple times. Attempts to loosen the drill bit by pulling up the drill string and the detonation of three small explosives [*Mortensen et al.*, 2009] caused some better SNR events. We tried to use these arrivals to verify whether our velocity model is reasonable. A relocated event, originating from an attempt to loosen the stuck drill string, is shown in Figures 2a–2c. The match between the well trajectory and the relocated hypocenter is within the location uncertainty.

Swarms 2 and 3 occur after periods when KT-40 was closed and reopened, and KJ-39 was closed in January and early February 2010. Swarm 4 matches the date when a fluid discharge test was performed on IDDP-1. KJ-39 was closed 6 days before this test.

We sporadically observe small-amplitude aftershocks in the coda of larger-amplitude earthquakes, but more frequently, we identify events with similar waveforms and magnitudes, sometimes separated only by a few seconds (Figure 3a). They share a common hypocenter location within error bars as well as near-identical source mechanism. We refer to them as multiplets, whose main differences consist of phase delays arising from slightly diverging ray paths. We performed waveform correlations on earthquakes identified by CMM and grouped those that had cross-correlation coefficients above 0.85 on at least two stations. Lower coefficients often retain earthquakes in a similar waveform group with hypocenter locations not explainable by the estimated ±150 m location uncertainty. A 4 s time window, starting at the *P* wave arrival, was chosen for correlation to include both *P* and *S* wave arrivals and some coda signal. We band-pass filtered the vertical component signals 2–18 Hz to reduce noise. On average, 32% (range 25–45%) of the earthquakes have at least one other similar event within our recording period. The wide percentage range mainly results from a few stations having significant data gaps at times. Figure 3a illustrates example waveforms of multiplets occurring within seconds of one another and that have their hypocenters located in the seismicity cluster A at 1.8 km depth bsl (Figures 2a–2c). Another example of multiplets that have longer interevent times is shown in Figure 3b. Seven matching signals are aligned in time and occurred weeks to months apart from one another as we found is typical. Their source location lies about 100 m SE of the IDDP-1 borehole at 1.5 km depth bsl.

The spatial clustering of events at Krafla allows us only to map magnitude distributions in specific areas within the caldera. We selected earthquakes within spheres of two sizes having diameters of 1.0 km and 1.5 km and centered at nodes separated by 125 m. No significant changes are observed regarding the choice of the two sphere sizes and cell node separation other than a smoothing effect. We separately prepared maps for the

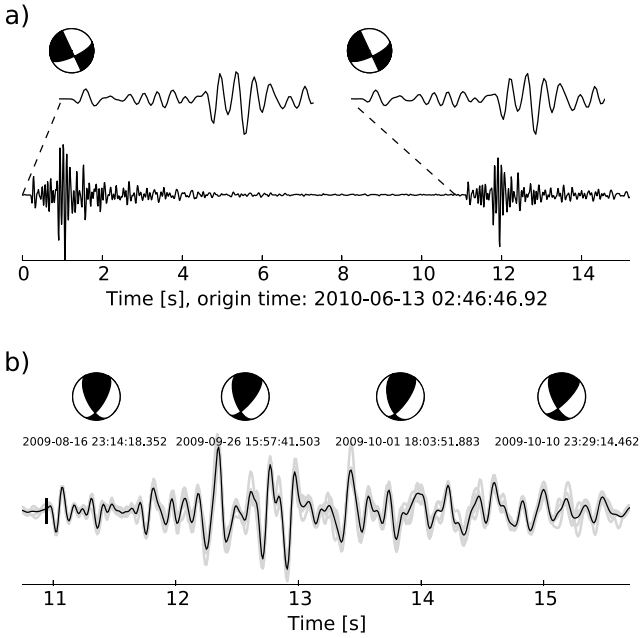

Figure 3. (a) Earthquakes with similar waveforms recorded at station K090 within seconds of one another. An enlarged signal window and the event focal mechanisms in lower hemisphere equal-area projection are displayed above. Black quadrants contain the tension axes. (b) Seven normalized waveforms from station K100 are aligned on a *P* wave arrival (vertical bar). Their ML range between −0.3 and 0.5. Black line represents the stacked waveform. Four well-constrained focal solutions of the events are shown above with their origin times.

319 day and 675 day long periods, because they have different network configurations and have average interstation distances of 1.5 km and 2.0 km, respectively. The majority of their *b* values match within their errors. Therefore, we measure no significant temporal *b* value change. Therefore, we cautiously combine the two earthquake catalogs to estimate the size distribution at each node using the higher $M_{min} = M_c - \Delta M/2$ value that resulted from the two separate time period analyses. An average M_{min} of -0.6 ± 0.1 and -0.1 ± 0.1 were estimated for all the nodes in the 319 and 675 day periods, respectively. We attribute the increased M_{min} for the later period mainly to the increased interstation spacing, because calculating M_{min} for shorter time segments within the two analysis periods and locally at selected nodes returned similar values. In Figure 4, the *b* value and error map is generated using the combined catalog of two recording periods. A sphere radius of 0.5 km and a minimum of 100 earthquakes per node were required for populating a node with a value. We observe elevated values at the edges of the colored patches, which are caused by rapidly decreasing earthquake numbers. The reduced number of events within the analysis volumes (spheres) correspond to increased errors in estimating *b*. Instead of selecting all events within an analysis volume, a constant number of events may be chosen randomly or with increasing time until a defined number is reached. This approach reduces edge effects, but may also select events distant from the node center that are then representing the size distribution of that node.

Kamer and Hiemer [2015] presented a *b* value estimation method that explores the model complexity given the data. An advantage of this approach is that every earthquake is used only once to compute a *b* value within a cell of a node. We select the models giving a better fit to the data than the initial model, which includes events of the entire region to calculate one *b* value. Instead of dividing the surface area into cells, we segment the depth profile, shown in Figure 4d, into cells such that we can apply the method in 2-D. All selected models are used then to build ensemble averaged *b* values. We found no significant spatial pattern. Likewise, selecting a test volume at the bottom of IDDP-1 did not return elevated *b* values above 1.

An average $b = 0.79 \pm 0.04$ ($-0.4 \leq \mathrm{ML} \leq 2.0$) of the entire region was estimated incorporating the entire recording period. We have removed events that significantly exceed the average daily event rate from the earthquake catalog (i.e., swarms) and recalculated the regional *b* value. A $\Delta\mathrm{AIC} < 2$ suggests that the removal of these earthquakes does not affect our regional estimate.

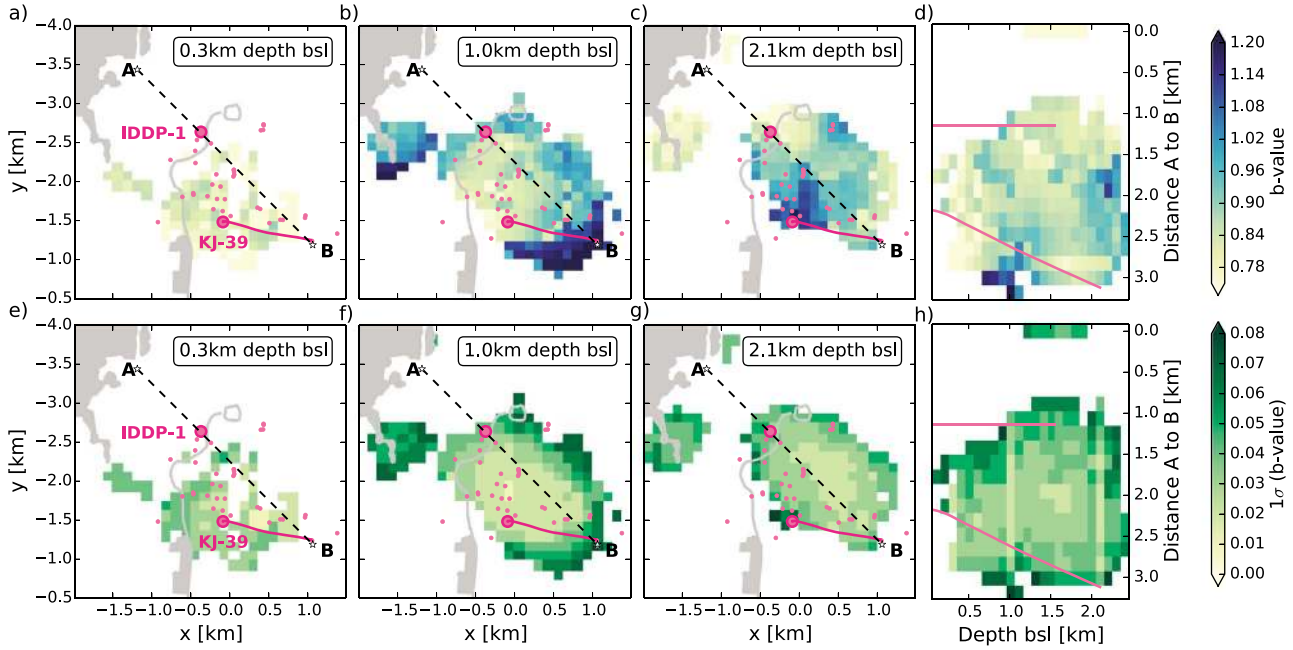

Figure 4. Size distribution map of the central Krafla caldera including data recorded between September 2009 and July 2012. The *b* values were estimated within spheres with radii 0.5 km around the cell nodes. The nodes, marked as squares, are separated by 125 m. A minimum number of 100 events was requested to populate a node. Surface locations of all geothermal wells and the trajectories of IDDP-1 and KJ-39, which both drilled into melt, are colored in pink.

Only events that have at least 12 polarity picks at distant stations are selected for further interpretation to ensure a minimum coverage of the focal spheres. More than three quarters of them are located deeper than 1.4 km bsl and the majority have magnitudes above −0.2. This is in agreement with our observation that larger-magnitude events occur closer to the depth of the peak seismic activity. Example DC solutions are illustrated in Figures 5a–5c with black lines indicating possible DC nodal planes and triangles marking the polarity picks (up or down) at different stations. On the sides of the hemisphere plots, lune source-type plots [*Tape and Tape*, 2013] allow us to visually relate the retrieved moment tensors to an appropriate physical source mechanism. The diagram's center, top, and bottom represent DC, purely explosive, and impulsive mechanisms, respectively. Colored dots show the PDF of the solution with red colors marking higher and blue lower probability. The PDF spread reveals that we need well-constrained focal solutions to uniquely assign a physical source mechanism to an event. Figures 5a and 5b show near-vertical dip slips, and Figure 5c a normal faulting mechanism. The latter is less well constrained and has two similarly fitting fault plane pairs with different strike directions. This event is counted as a DC mechanism, but its best fitting strike angle is not used further.

A ternary diagram (Figure 6a) provides some quantitative information about the DC faulting style of earthquake clusters. We assume close Andersonian faulting, although some nonoptimally oriented fault reactivations may lead to inaccurate faulting style representations on the ternary diagram [*Célérier*, 2010]. We find that most events in clusters A–D show normal faulting. Separately analyzing individual spatial clusters or grouping the events into different depth bins did not reveal a coherent change of pattern. We followed *Frohlich* [2001] in dividing the focal solutions into four different regimes: normal, reverse, strike slip, and *odd*. Few solutions exhibit strike slip or reverse faulting characters. Solutions that do not fall into a corner region are termed odd and represent oblique-slip on steep planes or strike slip on low-dipping planes. Several of these odd solutions are found close to the *T* axis with near-vertical or near-horizontal nodal planes. Rose diagrams of their strike directions, grouped according to their spatial clusters, present a diverse distribution (Figures 6b–6d). In cluster D, the strikes are mostly parallel in northeastern and southern directions. Clusters A and B are not as clear, but we have here only a few data points.

The estimated strike, dip, and rake information were inverted to obtain a uniform stress field orientation for clusters A and B (Figure 7). The grouping of spatially separate event clusters was performed visually. Cluster D in Figure 2a is split into a northwestern (D-NW) and southeastern (D-SE) part. We randomly selected one of the two fault planes to be the correct one. Cluster D-NW mainly covers the surface area between boreholes

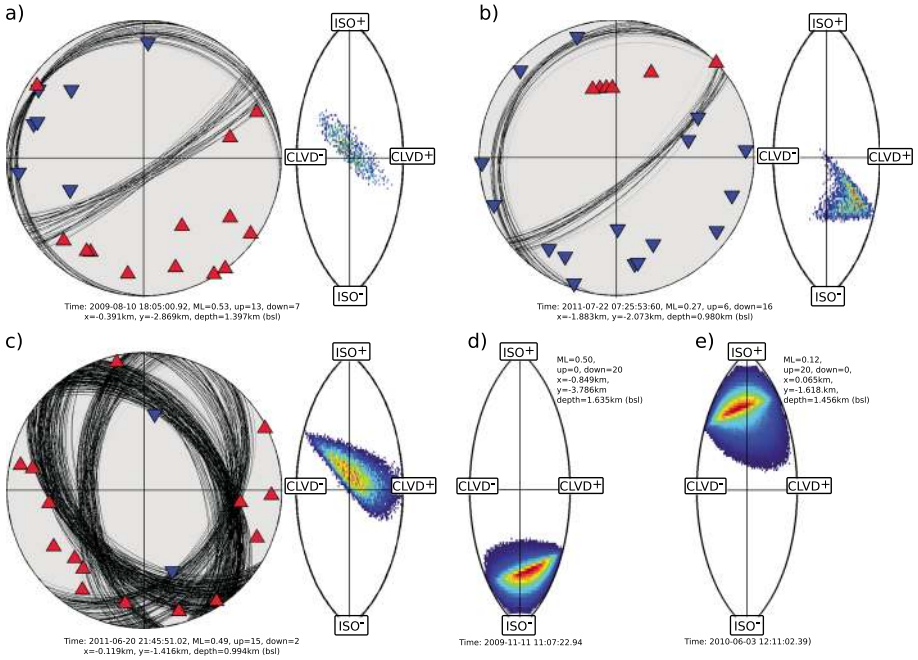

Figure 5. (a–c) DC focal mechanisms displayed in lower hemisphere projections on their left, with stations (triangles) indicating their polarity picks (up, down) of the arriving waveforms. Black lines show the distribution of possible fault planes for DC-constrained solutions. On their right, lune source-type plots [*Tape and Tape*, 2013] of the PDF are plotted with blue colors corresponding to low and red to high probability. (d) Illustration of a strongly implosive event and (e) an explosive event with all arrivals having the same polarities. Details of the event magnitudes and locations are given below subfigures in Figures 5a–5c and on their sides in Figures 5d–5e.

KJ-26 and IDDP-1. Figures 7b–7e show the stress inversion results along with the *P* and *T* axes of the individual earthquakes. Colored points in the background represent solutions that are obtained by bootstrap resampling the data set. Large spreads correspond to less constrained solutions of $s_{1,2,3}$. The two separate clusters A and B show similar principal stress axis directions, but only a few events are selected. The principal axes cannot be resolved clearly for D-NW and are weakly constrained for D-SE. In all areas the largest compressive stress direction (s_1) is near vertical. The s_2 and s_3 in the D subclusters, however, appear to have similar magnitudes, which are reflected in the relatively high value of *R* as well as in the wide distribution of the s_2 and s_3 solutions generated during the bootstrap resampling.

5.1. Non-Double-Couple Mechanisms

About 10% of events in cluster A, 17% in cluster B, and 18% in cluster D show non-DC source mechanisms. Cluster C had only a handful of events. We obtain these numbers by visually checking the lower hemisphere projections of forced DC solutions and also the spread of uncertainty (95% contour interval) in the lune source-type plots. We only counted an event as non-DC, if the 95% contour interval of the uncertainty map did not overlap with the DC point in the lune plot. Sole inspection of the lune diagram would, of course, not allow a decision to be made as to whether an event is DC or not. We may have picked only positive polarities in the compressional, or negative polarities in the dilatational, quadrants indicating a pure isotropic source in the lune plot, although it may be a DC event. We further find that one third of the non-DC events in cluster A, 18% in cluster B, and 30% in cluster D show negative volumetric components.

Locations of sources with large volumetric changes and no opposite polarity picks are shown in Figures 2a–2c. Most non-DC sources are explosive, with only two being implosive. We note that these events lie locally below the deepest points of the nearest boreholes.

6. Discussion

The seismicity in 2009–2012 was governed by small-magnitude events during a volcanically quiet period. An estimated 32% of the earthquakes are repeating events. This clustering rate fits well the rates of 24–37%

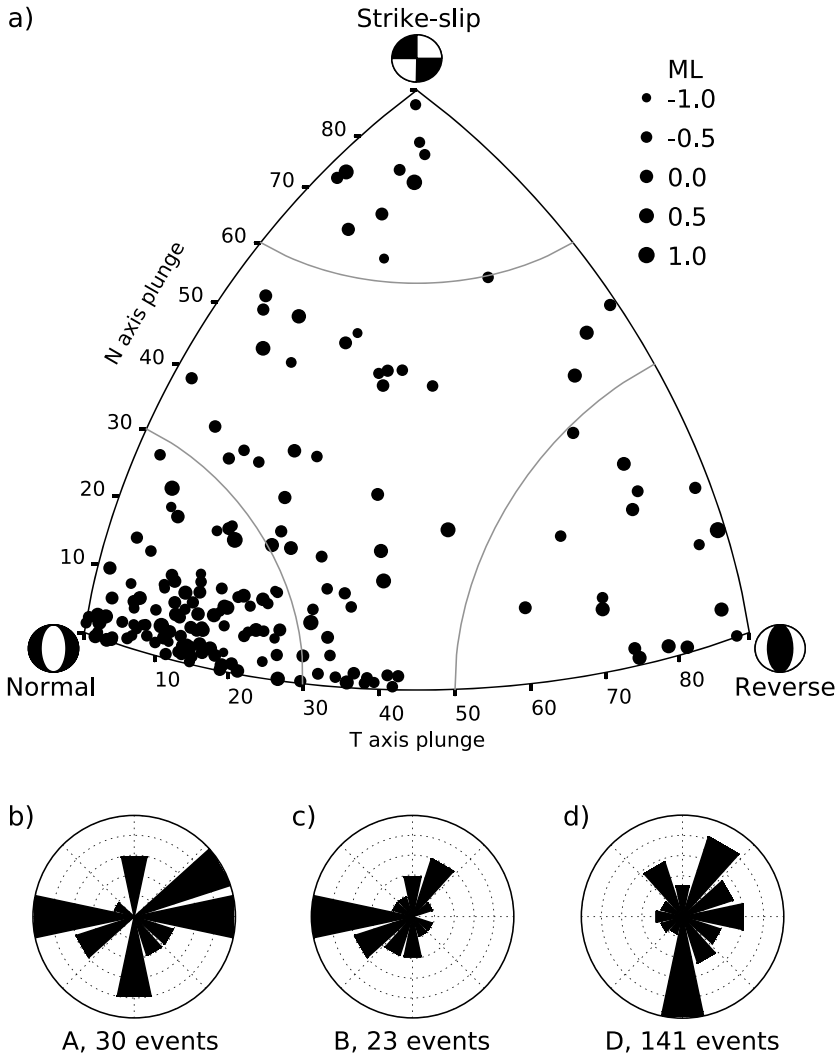

Figure 6. (a) Equal-area projection, after *Kaverina et al.* [1996], displaying the distribution of 182 well-constrained DC focal mechanisms (dots). Dot sizes are scaled relative to their event magnitudes. Compressed quadrants of the beach ball plots are colored black. Following *Frohlich* [2001], we further delineate corner regions in which faulting mechanisms are considered predominantly as normal, reverse (thrust), and strike slip. Curved lines indicate where the *P*, *N*, and *T* axes lie within 30°, 30°, and 40° of the vertical, respectively. (b–d) Rose diagrams that show the strike directions of well-constrained DC nodal planes. Cluster letters and number of events are given below the plots.

reported from other active volcanic caldera systems, which have events with similar magnitudes [*Massin et al.*, 2013, and references therein]. The nonrepeating events may represent ruptures of partially healed preexisting faults or intact rock. Considering the magnitudes of our events, typical source dimensions of up to a few tens of meters can be expected [*Wyss and Brune*, 1968]. Circulating geothermal fluids possibly limit crack propagation during earthquake ruptures and hence their size [*Foulger and Long*, 1984]. We find a weak correlation between increased numbers of multiplets and swarms. The average magnitudes of repeating events is 0.1 ± 0.5 (2061 events) and for swarms -0.2 ± 0.4 (703 events). The weak correlation between increased numbers of multiplets and swarms is used sometimes to argue that the locally modified stresses leading to swarms reactivated preexisting faults.

We observe that swarms often occur simultaneously or days after fluids have been injected, the injection rate changed, or circulation losses occurred while drilling. Fluid reinjection started in 2002 at Krafla, partly in an attempt to sustain reservoir pressure. *Ágústsson et al.* [2012] noted that induced seismicity occurred as soon as more than 0.04–0.06 m^3/s were injected at Krafla. Circulation fluids lost during drilling reached volumes of up to 0.04 m^3/s [*Mortensen et al.*, 2009]. We also observe elevated seismicity when larger volumes are injected.

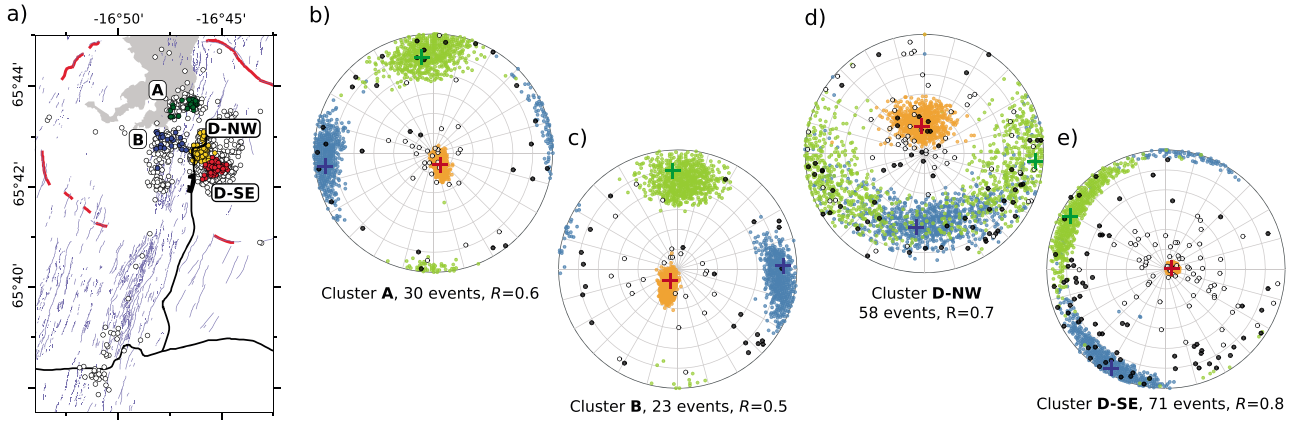

Figure 7. (a) Map showing the hand-picked earthquake epicenters (circles), fissures (purple lines, after *Hjartardóttir et al.* [2012]) used as a proxy of the rift axis, caldera rim (red), and the dike zone (green) of the Krafla fires. (b–e) Lower hemisphere equal-area projection of *P* (open circles) and *T* (black solid points) axes of well-constrained DC events for clusters A, B, D-NW, and D-SE. The selected events are highlighted in Figure 7a. Red ($\vec{s}_1$), green ($\vec{s}_2$), and blue ($\vec{s}_3$) crosses represent the best fitting principal stress axes. *R* is the relative stress magnitude. Color-coded circles mark stress axes solutions obtained by bootstrap resampling 1000 times.

Small injection volumes probably cause smaller magnitude events or aseismic slip. We observe little swarm activity during periods when little or no change in fluid balance occurs. This suggests that fluids are likely candidates for the triggering microearthquakes. In the case of injections, fluids locally increase the pore pressure and reduce the effective normal stresses on nearby faults and so bring them closer to failure [*Raleigh et al.*, 1976].

6.1. Earthquake Size Distribution

Our *b* values (Figure 4) of the Krafla caldera indicate normal crustal values, which match the findings of *Arnott and Foulger* [1994a] 20 years earlier. It appears that the *b* values are not elevated despite the presence of melt at shallow depth, associated high geothermal gradients and pore pressures, and sequences of extensively fractured rocks. Possibly we are observing the third stage of the characteristic *b* value sequence, described earlier, where intrusive melt has been sitting in the crust for some time and the initially increased pore pressure due to magmatic degassing and hot geothermal fluids has reached a relatively constant level. In the case of a long-lived melt body beneath Krafla, the concentrated stress introduced during earlier dike formation may have been dissipated through on-going rifting. An alternative explanation for the low *b* values is that the melt pockets are small localized features that do not cause increased small-magnitude seismicity. However, this would not be in agreement with tomographic images [e.g., *Schuler et al.*, 2015] and the fact that heat is expelled over large surface areas. Our preferred explanation therefore is a larger single, or multiple smaller melt bodies, embedded in a hot and plastically behaving crust.

6.2. Double-Couple Earthquakes

Most of the focal solutions in Figure 6a exhibit normal faulting characteristics. The strike azimuths (Figures 6b–6d) appear scattered, but nonetheless show a slight dominance in NE-SW and E-W directions. Both observations agree with results presented by *Arnott and Foulger* [1994b]. A fast shear wave polarization analysis by *Tang et al.* [2008] found two preferred fast-polarization directions, N-S and E-W, which were interpreted as two fracture systems oriented perpendicular to each other.

Inverting focal solutions for a uniform stress field has limitations. A uniform stress field is perhaps a good assumption in some regions [*Zoback and Zoback*, 1980], but may give meaningless results in others [*Smith and Heaton*, 2006]. If a new fault plane develops in isotropic rock with a uniform background stress field, the *P* and *T* axes may give an indication of $\vec{s}_1$ and $\vec{s}_3$, respectively. In more realistic settings, slip frequently occurs on nonoptimally oriented, preexisting planes of weaknesses. We find that at least one third of events at Krafla are repeating events. *Célérier* [2008] proposed that reactivated faults are more likely to be near-optimally oriented if they plot closer to the corners in a ternary diagram (Figure 6a). However, selecting only these events to invert for stress directions would reduce the focal diversity needed to solve for the principal stress axes.

Wyss et al. [1992] argue that it is reasonable to assume a uniform stress field if subvolumes of data return similar results. The small number of earthquakes prevents us from dividing our clusters into smaller volumes

except for cluster D. Clusters A and B exhibit similar stress orientations with s_1 pointing vertically down and s_3 being parallel to the spreading direction. These axis orientations coincide with the classical model of an extensional tectonic stress regime where $\sigma_1 \simeq \sigma_2 > \sigma_3$. Similar results have been reported from other parts of the rift axis [e.g., *Klein et al.*, 1977; *Foulger*, 1988]. Hydrofracturing borehole stress measurements in east Iceland show that the maximum horizontal stress is subparallel to the nearest fissure swarms in the axial rift zone and thus the minimum horizontal stress is subparallel to the spreading direction [*Haimson and Rummel*, 1982]. They also show that horizontal stresses increase slowly with depth and that the vertical stress becomes larger at a few hundred meters depth, leading to optimal conditions for normal faulting. Borehole pressure logs from IDDP-1 show a pivot point at 1.95 km depth with a pressure of 15.5 MPa [*Friðleifsson et al.*, 2015]. The pivot point, usually representing the depth of the dominating formation feeding zone, determines the formation pressure at that depth. Near crystallizing and cooling magma walls, significant tensile stresses may develop with $\vec{s}_3$ perpendicular to the lithostatic load, whereas below the brittle-plastic transition we expect the lithostatic load to become σ_3 due to the deformation in response to buoyancy [*Fournier*, 1999].

Cluster D-NW and D-NE exhibit near-vertical s_1, but s_2 and s_3 appear to be different than in clusters A and B (Figure 7). Cluster D-NW is especially unconstrained as is indicated by the large spread of solutions generated during bootstrap resampling. Perhaps this shows that $\sigma_2 \approx \sigma_3$. In contrast to the volumes of clusters A and B, D mostly encompasses the exploited geothermal field undergoing fluid injections/withdrawals. Two active wells, KJ-26 and IDDP-1, both penetrate the volume of cluster D-NW. Earthquakes used for our stress analysis all originate from a similar depth range, which is dominated by intrusives at the IDDP-1 site. In contrast to our horizontal stress change indications, *Martínez-Garzón et al.* [2013] reported vertical stress changes between reservoir and adjacent host rock at The Geysers likely induced by poroelastic or thermoelastic stressing. Around producing fractures, where strong temperature and pressure gradients are expected, thermoelastic effects may dominate over poroelastic effects and alter the stress state within the reservoir [*Segall and Fitzgerald*, 1998].

For the Bjarnarflag-Námafjall field and the dike zone, *Arnott and Foulger* [1994b] found just after the Krafla fires rifting episode that the stress orientations were highly variable and $\vec{s}_1$ was perpendicular to the rift axis. The latter was possibly caused by multiple intrusions and caused $\vec{s}_1$ to rotate from vertical to horizontal. About 20 years after the Krafla fires and about 5 km to the north along the rift axes, we find $\vec{s}_1$ vertical inside and outside the main exploited geothermal field. $\vec{s}_3$ is nearly aligned with the spreading direction outside the main geothermal field and oriented as imagined during an interrifting period [*Arnott and Foulger*, 1994b]. *Bergerat et al.* [1990] and *Plateaux et al.* [2012] also found s_3 aligned parallel to the plate divergence direction both in and off the rift zone for locations to the north, south, and east of Krafla. The horizontal stress axes in the lower part of the productive field suggest $\sigma_2 \approx \sigma_3$. We know further from geodetic measurements [*Ali et al.*, 2014] that the observed surface deformation is attributed to the half-spreading rate of 9 mm/yr of the plates, viscoelastic relaxation deriving from the Krafla fires, and a shallow deflating magma reservoir. Therefore, the local stress field may be affected by a more complex interaction of different stress sources.

If we apply the deformation rate interpretation of slip inversion data, the global *P* and *T* axes are not interpreted as $\vec{s}_1$ and $\vec{s}_3$ but instead as the most and least compressive deformation rate directions. The smallest deformation rate axis is closely aligned with the spreading direction in clusters A and B, somewhat diffuse in D-NW, and parallel to the rift in D-SE. Local fault block rotations during slip are not considered here.

6.3. Non-Double-Couple Earthquakes

A large proportion of events are consistent with non-shear-faulting behavior. Similar to previous studies, we found numerous nonshear events at Krafla interspersed with DC earthquakes. However, we classified less than 20% as distinct nonshear events, of which most are explosive and have magnitudes between −0.3 and 0.6. In comparison to some other studies, we believe this low percentage partly derives from including uncertainties in the moment tensor inversion and partly because we sometimes suffer from sparse focal coverage. Nevertheless, there is tensile and tensile-shear faulting occurring close to the brittle-plastic transition. Ground water is heated and expands to a high-pressured and superheated fluid near the melt leading to hydraulic fracturing and brecciation. Exsolving magmatic fluids, comprising hypersaline brine and steam, are expected to cross the brittle-plastic interface on occasion. Pore pressures in the plastic rock are equal to the lithostatic load but are hydrostatic in the brittle environment, which will cause the fluid to expand and transform to superheated steam when moving into the brittle part [*Fournier*, 1999]. The decompression causes brecciation, an increase in the strain rate, and stress difference in the plastic rock due to increased fluid movement across

the brittle-plastic interface [*Fournier*, 1999]. The fact that superheated fluids are extracted from a highly productive zone overlying melt suggests that this is a reasonable conceptual model for this zone. The non-DC earthquakes are expected to occur in this zone, where fluid can change the ambient stress locally, and cracks may open or close, or even remain open.

We recorded two mainly implosive events that might be related to thermal contraction of cooling magma [*Foulger and Long*, 1984; *Miller et al.*, 1998] underneath. One of these implosive events is less than 300 m south of IDDP-1 and therefore close to where we expect the melt-rock interface to lie (Figures 2a–2c). The second is located at the bottom of the seismicity cluster A to the NW, which shows the same characteristic seismicity distribution as at IDDP-1. Thus, we believe that this event is also located close to an underlying melt zone. This is supported by tomographic images [*Schuler et al.*, 2015]. A source dominated by near-vertical single force or a vertical-CLVD mechanism might produce only dilatational first motions as well at the stations, but this presumes that there is a small region at the surface where we could have recorded compressional first motions. Physical sources for such mechanisms may include fluid movement or cone-shaped fault structures [*Shuler et al.*, 2013]. Although we cannot rule out such an alternative explanation, we stick with the simple implosive source explanation. Fluid motions, phase changes, mixing of meteoric and magmatic fluids, and cooling of the underlying magma pocket are likely to be responsible for the variety of DC and non-DC earthquakes. Seismogenic faulting within the highly viscous silicic magma may also produce earthquakes with magnitudes that would be observable with our network [*Tuffen et al.*, 2008]. However, our location uncertainties do not allow us to pinpoint the hypocenters exactly to one stratigraphic layer, because the whole vertical sequence at the bottom of IDDP-1, comprising dolerites, granophyres (highly productive zone), and rhyolitic melt is only about 100 m thick.

On a final note, crustal anisotropy has not been considered in our tomographic model nor in our focal mechanism inversions. We expect, however, from shear wave splitting measurements [*Tang et al.*, 2008] and from the aligned fractures in the extensive fissure system at the surface, that the crustal fabric is anisotropic. This in turn must affect our moment tensor inversion [*Vavryčuk*, 2005]. We have not included nor assessed this uncertainty yet.

7. Conclusion

The microseismicity within the Krafla caldera between 2009 and 2012 is concentrated near geothermal fields in the upper 2–3 km. The depth with the largest number of earthquakes above the magnitude of completeness matches the depth of the rock-melt interface at the IDDP-1 borehole. The relative size distributions of events (b value) are not elevated close to the melt, but rather show average crustal values of $b \leq 0.9$. Although this is a period of volcanic quiescence, a few small-magnitude earthquake swarms were detected at locations and times suggesting that geothermal fluids are important in the triggering processes. A weak correlation between swarms and repeating earthquakes is interpreted as stress activation of preexisting faults. About 32% of the events are found to be repeating earthquakes.

Focal solutions of earthquakes suggest that less than about 20% deviate significantly from shear-faulting mechanisms. Most non-shear-faulting mechanisms involve positive volume changes and only two were implosive events. The proximity of these events to the expected melt-rock interface depth suggests that geothermal fluids play an important role in their source processes. We surmise that they occurred in the superheated steam zone above the melt. The double-couple earthquakes, on the other hand, mostly represent normal faulting styles. Estimated P and T axes were used to infer the principal stress or deformation rate axes. We find that the maximum compressive stress (deformation rate) axis is always vertical. The least compressive stress (deformation rate) direction is closely aligned with the plate spreading direction outside the main geothermal field and is not well defined inside it. Here the relative horizontal stress (deformation rate) magnitudes are similar.

Acknowledgments
We thank Julian Drew for the use of his CMM algorithm and Jon Tarasewicz for acquiring the bulk of the field data. Seismometers were borrowed from SEIS-UK under loan 891, with additional data from SIL network stations operated by the Icelandic Meteorological Office. The data will be stored at IRIS (www.iris.edu) and accessible from there. The Natural Environment Research Council UK funded the fieldwork. Landsvirkjun supported the field campaigns and provided borehole information. We thank two anonymous reviewers for critically reading this paper. J.S. also thanks Y. Kamer and S. Hiemer for discussing parts of their b value method. Data were mainly processed using the ObsPy package and visualized using Matplotlib and Generic Mapping Tools. Cambridge University Department of Earth Sciences contribution number ESC.3672. J.S. was supported by the Swiss National Science Foundation.

References

Ágústsson, K., Ó. G. Flóvenz, Á. Guðmundsson, and S. Árnadóttir (2012), Induced seismicity in the Krafla high temperature field, *GRC Trans.*, *36*, 975–980.

Akaike, H. (1974), A new look at the statistical model identification, *IEEE Trans. Autom. Control*, *19*, 716–723.

Ali, S. T., K. L. Feigl, B. B. Carr, T. Masterlark, and F. Sigmundsson (2014), Geodetic measurements and numerical models of rifting in Northern Iceland for 1993–2008, *Geophys. J. Int.*, *196*, 1267–1280.

Ármansson, H., B. Gudmundsson, and B. S. Steingrímsson (1987), Exploration and development of the Krafla geothermal area, *Joekull*, *37*, 13–29.

Árnason, K., A. M. Vilhjálmsson, and T. Björnsdóttir (2009), A study of the Krafla volcano using gravity, micro earthquake and MT data, paper presented at Short Course IV on Exploration for Geothermal Resources, UNU-GTP, KenGen and GDC, United Nations Univ., Kenya, 1–22 Nov.

Arnott, S., and G. Foulger (1994a), The Krafla spreading segment, Iceland: 1. Three-dimensional crustal structure and the spatial and temporal distribution of local earthquakes, *J. Geophys. Res.*, *99*, 23,801–23,825.

Arnott, S., and G. Foulger (1994b), The Krafla spreading segment, Iceland: 2. The accretionary stress cycle and nonshear earthquake focal mechanisms, *J. Geophys. Res.*, *99*, 23,827–23,842.

Bergerat, F., J. Angelier, and T. Villemin (1990), Fault systems and stress patterns on emerged oceanic ridges: A case study in Iceland, *Tectonophysics*, *179*, 183–197.

Björnsson, A., G. Johnsen, S. Sigurdsson, and G. Thorbergsson (1979), Rifting of the plate boundary in North Iceland 1975–1978, *J. Geophys. Res.*, *84*, 3029–3038.

Boore, D. M. (2003), Simulation of ground motion using the stochastic method, *Pure Appl. Geophys.*, *160*, 635–676.

Bormann, P., S. Wendt, and D. Di Giacomo (2013), Summary of magnitude working group recommendations on standard procedures for determining earthquake magnitudes from digital data, IASPEI.

Brandsdóttir, B., and P. Einarsson (1979), Seismic activity associated with the September 1977 deflation of the Kralfa central volcano in northeastern Iceland, *J. Volcanol. Geotherm. Res.*, *6*, 197–212.

Brandsdóttir, B., and W. Menke (1992), Thin low-velocity zone within the Krafla caldera, NE-Iceland attributed to a small magma chamber, *Geophys. Res. Lett.*, *12*, 2381–2384.

Brandsdóttir, B., W. Menke, P. Einarsson, R. S. White, and R. K. Staples (1997), Färoe-iceland ridge experiment 2. Crustal structure of the Krafla central volcano, *J. Geophys. Res.*, *102*, 7867–7886.

Buck, W. R., P. Einarsson, and B. Brandsdóttir (2006), Tectonic stress and magma chamber size as controls on dike propagation: Constraints from the 1975–1984 Krafla rifting episode, *J. Geophys. Res.*, *111*, B12404, doi:10.1029/2005JB003879.

Célérier, B. (2008), Seeking Anderson's faulting in seismicity: A centennial celebration, *Rev. Geophys.*, *46*, RG4001, doi:10.1029/2007RG000240.

Célérier, B. (2010), Remarks on the relationship between the tectonic regime, the rake of the slip vectors, the dip of the nodal planes, and the plunges of the P, B, and T axes of earthquake focal mechanisms, *Tectonophysics*, *482*, 42–49.

Chouet, B. A. (1996), Long-period volcano seismicity: Its source and use in eruption forecasting, *Nature*, *380*, 309–316.

Drew, J., R. S. White, F. Tilmann, and J. Tarasewicz (2013), Coalescence microseismic mapping, *Geophys. J. Int.*, *195*, 1773–1785.

Einarsson, P. (1978), S-wave shadows in the Krafla caldera in NE-Iceland, evidence for a magma chamber in the crust, *Bull. Volcanol.*, *41*, 187–195.

Einarsson, P. (1991), Earthquakes and present-day tectonism in Iceland, *Tectonophysics*, *189*, 261–279.

Einarsson, P., and B. Brandsdóttir (1980), Seismological evidence for lateral magma intrusion during the July 1978 deflation of the Krafla volcano in NE-Iceland, *J. Geophys.*, *47*, 160–165.

Elders, W., et al. (2011), Origin of a rhyolite that intruded a geothermal well while drilling at the Krafla volcano, *Geology*, *39*, 231–234.

Farell, J., S. Husen, and R. B. Smith (2009), Earthquake swarm and *b*-value characterization of the Yellowstone volcano-tectonic system, *J. Volcanol. Geotherm. Res.*, *188*, 260–276.

Fournier, R. O. (1999), Hydrothermal processes related to movement of fluid from plastic into brittle rock in the magmatic-epithermal environment, *Econ. Geol.*, *94*, 1193–1211.

Foulger, G. R. (1988), Hengill triple junction, SW Iceland: Anomalous earthquake focal mechanisms and implications for process within the geothermal reservoir and at accretionary plate boundaries, *J. Geophys. Res.*, *93*, 13,507–13,523.

Foulger, G. R., B. R. Julian, D. P. Hill, A. M. Pitt, P. E. Malin, and E. Shalev (2004), Non-double-couple microearthquakes at Long Valley caldera, California, provide evidence for hydraulic fracturing, *J. Volcanol. Geotherm. Res.*, *132*, 45–71.

Foulger, G. R., and R. E. Long (1984), Anomalous focal mechanisms: Tensile crack formation on an accreting plate boundary, *Nature*, *310*, 43–45.

Friðleifsson, G. O., B. Pálsson, A. L. Albertsson, B. Stefánsson, E. Gunnlaugsson, J. Ketilsson, and P. Gíslason (2015), IDDP-1 drilled into magma—World's first magma-EGS system created, paper presented at World Geothermal Congress 2015, Melbourne, Australia.

Frohlich, C. (1994), Earthquakes with non-double-couple mechanisms, *Science*, *264*, 804–809.

Frohlich, C., and S. Davis (1993), Teleseismic b-values: Or, much ado about 1.0, *J. Geophys. Res.*, *98*, 631–644.

Frohlich, C. (2001), Display and quantitative assessment of distributions of earthquake focal mechanisms, *Geophys. J. Int.*, *144*, 300–308.

Gutenberg, R., and C. F. Richter (1944), Frequency of earthquakes in California, *Bull. Seismol. Soc. Am.*, *34*, 185–188.

Haimson, B. C., and F. Rummel (1982), Hydrofracturing stress measurements in the Iceland research drilling project drill hole at Reydarfjordur, Iceland, *J. Geophys. Res.*, *87*, 6631–6649.

Hardebeck, J. L., and A. J. Michael (2006), Damped regional-scale stress inversions: Methodology and examples for southern California and the Coalinga aftershock sequence, *J. Geophys. Res.*, *111*, B11310, doi:10.1029/2005JB004144.

Heaton, T. H. (1990), Evidence for and implications of self-healing pulses of slip in earthquake rupture, *Phys. Earth Planet. Inter.*, *64*, 1–20.

Hole, J. A., and B. C. Zelt (1995), 3-D finite-difference reflection traveltimes, *Geophys. J. Int.*, *121*, 427–434.

Hjartardóttir, Á. R., P. Einarsson, E. Bramham, and T. J. Wright (2012), The Krafla fissure swarm, Iceland, and its formation by rifting events, *Bull. Volcanol.*, *74*, 2139–2153.

Ishimoto, M., and K. Iida (1939), Observations of earthquakes registered with the microseismograph constructed recently, *Bull. Earthquake Res. Inst.*, *17*, 443–478.

Jacobs, K. M., E. G. C. Smith, M. K. Savage, and J. Zhuang (2013), Cumulative rate analysis (CURATE): A clustering algorithm for swarm dominated catalogs, *J. Geophys. Res. Solid Earth*, *118*, 553–569, doi:10.1029/2012JB009222.

Jónasson, K. (2007), Silicic volcanism in Iceland: Composition and distribution within the active volcanic zones, *J. Geodyn.*, *43*, 101–117.

Julian, B. R., A. D. Miller, and G. R. Foulger (1998), Non-double couple earthquakes, *Rev. Geophys.*, *36*, 525–549.

Kamer, Y., and S. Hiemer (2015), Data-driven spatial *b* value estimation with applications to California seismicity: To *b* or not to *b*, *J. Geophys. Res. Solid Earth*, *120*, 5191–5214, doi:10.1002/2014JB011510.

Kaverina, A. N., A. V. Lander, and A. G. Prozorov (1996), Global creepex distribution and its relation to earthquake-source geometry and tectonic origin, *Geophys. J. Int.*, *125*, 249–265.

Klein, F. W., P. Einarsson, and M. Wyss (1977), The Reykjanes Peninsula, Iceland, earthquake swarm of September 1972 and its tectonic significance, *J. Geophys. Res.*, *82*, 865–887.

Maeda, Y., H. Kumagai, R. Lacson Jr., M. S. Figueroa II, and T. Yamashina (2013), Source process of long-period seismic events at Taal volcano, Philippines: Vapor transportation and condensation in a shallow hydrothermal fissure, *J. Geophys. Res. Solid Earth*, *118*, 2832–2846, doi:10.1002/jgrb.50205.

Martínez-Garzón, P., M. Bohnhoff, G. Kwiatek, and G. Dresen (2013), Stress tensor changes related to fluid injection at The Geysers geothermal field, California, *Geophys. Res. Lett.*, *40*, 2596–2601, doi:10.1002/grl.50438.
Massin, F., J. Farell, and R. B. Smith (2013), Repeating earthquakes in the Yellowstone volcanic field: Implications for rupture dynamics, ground deformation, and migration in earthquake swarms, *J. Volcanol. Geotherm. Res.*, *257*, 159–173.
McKenzie, D. P. (1969), The relation between fault plane solutions for earthquakes and the directions of the principal stresses, *Bull. Seismol. Soc. Am.*, *59*, 591–601.
McNutt, S. R. (2005), Volcanic seismology, *Annu. Rev. Earth Planet. Sci.*, *33*, 461–491.
Miller, A. D., G. R. Foulger, and B. R. Julian (1998), Non-double-couple earthquakes, 2. Observations, *Rev. Geophys.*, *36*, 551–568.
Miller, A. D., B. R. Julian, and G. R. Foulger (1998), Three-dimensional seismic structure and moment tensors of non-double-couple earthquakes at the Hengill-Grensdalur volcanic complex, Iceland, *Geophys. J. Int.*, *133*, 309–325.
Mogi, K. (1962), Magnitude-frequency relation for elastic shocks accompanying fractures of various materials and some related problems in earthquakes, *Bull. Earthquake Res. Inst.*, *40*, 831–853.
Mortensen, A. K., Þ. Egilson, B. Gautason, S. Árnadóttir, and Á. Guðmundsson (2014), Stratigraphy, alteration mineralogy, permeability and temperature conditions of well IDDP-1, Krafla, NE-Iceland, *Geothermics*, *49*, 31–41.
Mortensen, A. K., K. Grönvold, Á Gudmundsson, B. Steingrímsson, and T. Egilson (2010), Quenched silicic glass from well KJ-39 in Krafla, north-eastern Iceland, paper presented at World Geothermal Congress 2010, Bali, Indonesia.
Mortensen, A. K., M. Á. Sigurgeirsson, Þ. Egilson, G. H. Guðfinnsson, H. Tryggvason, R. B. Jónsson, and S. Sveinbjörnsson (2009), Krafla âĂŞ Hola KT-40. 3. áfangi: Jarðlagagreining og mælingar. Krafla - borehole KT-40, 3rd section: Borehole geology and geophysical measurements, íSOR-2009/70, LV-2009/144, 1–24.
Plateaux, R., F. Bergerat, N. Béthoux, T. Villemin, and M. Gerbault (2012), Implications of fracturing mechanisms and fluid pressure on earthquakes and fault slip data in the east Iceland rift zone, *Tectonophysics*, *581*, 19–34.
Pugh, D. J., R. S. White, and P. A. F. Christie (2016), A Bayesian method for microseismic source inversion, *Geophys. J. Int.*, *206*(2), 1009–1038. doi:10.1093/gji/ggw186.
Raleigh, C. B., J. H. Healy, and J. D. Bredehoeft (1976), An experiment in earthquake control at Rangley, Colorado, *Science*, *191*, 1230–1237.
Rivera, L., and H. Kanamori (2002), Spatial heterogeneity of tectonic stress and friction in the crust, *Geophys. Res. Lett.*, *29*(6), 1088, doi:10.1029/2001GL013803.
Ross, A., G. R. Foulger, and B. R. Julian (1999), Source processes of industrially-induced earthquakes at The Geysers geothermal area, California, *Geophys.*, *64*, 1877–1889.
Sæmundsson, K. (1979), Outline of the geology of Iceland, *Jokull*, *29*, 7–28.
Scholz, C. H. (1968), The frequency-magnitude relation of microfracturing in rock and its relation to eathquakes, *Bull. Seismol. Soc. Am.*, *58*, 399–415.
Schorlemmer, D., and S. Wiemer (2014), Earthquake statistics at Parkfield: 1. Stationarity of b values, *J. Geophys. Res.*, *109*, doi:10.1029/2004JB003234.
Schorlemmer, D., S. Wiemer, and M. Wyss (2005), Variations in earthquake-size distribution across different stress regimes, *Nature*, *437*, 539–542.
Schuler, J., P. A. F. Christie, and R. S. White (2014), Borehole study of compressional and shear attenuation of basalt flows penetrated by the Brugdan and William wells on the Faroes shelf, *Geophys. Prospect.*, *62*, 315–332.
Schuler, J., T. Greenfield, R. S. White, S. W. Roecker, B. Brandsdóttir, J. M. Stock, J. Tarasewicz, H. R. Martens, and D. J. Pugh (2015), Seismic imaging of the shallow crust beneath the Krafla central volcano, NE Iceland, *J. Geophys. Res. Solid Earth*, *120*, 7156–7173, doi:10.1002/2015JB012350.
Segall, P., and S. D. Fitzgerald (1998), A note on induced stress changes in hydrocarbon and geothermal reservoirs, *Tectonophysics*, *289*, 117–128.
Shi, Y., and B. A. Bolt (1982), The standard error of the magnitude-frequency *b*-value, *Bull. Seism. Soc. Am.*, *72*, 1677–1687.
Shuler, A., G. Ekström, and M. Nettles (2013), Physical mechanisms for vertical-CLVD earthquakes at active volcanoes, *J. Geophys. Res. Solid Earth*, *118*, 1569–1586, doi:10.1002/jgrb.50131.
Smith, D. E., and T. Heaton (2006), Models of stochastic, spatially varying stress in the crust compatible with focal-mechanism data, and how stress inversions can be biased toward the stress rate, *Bull. Seismol. Soc. Am.*, *101*, 1396–1421.
Sykes, L. R. (1970), Earthquake swarms and sea-floor-spreading, *J. Geophs. Res.*, *75*, 6598–6611.
Tang, C., J. A. Rial, and J. M. Lees (2008), Seismic imaging of the geothermal field at Krafla, Iceland, using shear-wave splitting, *J. Volcanol. Geotherm. Res.*, *176*, 315–324.
Tape, W., and C. Tape (2013), The classical model for moment tensors, *Geophys. J. Int.*, *195*, 1701–1720.
Tinti, S., and F. Mulargia (1987), Confidence intervals of *b* values for grouped magnitudes, *Bull. Seismol. Soc. Am.*, *77*, 2125–2134.
Tuffen, H., R. Smith, and P. R. Sammonds (2008), Evidence for seismogenic fracture of silicic magma, *Nature*, *453*, 511–514.
Twiss, R. J., and J. R. Unruh (1998), Analysis of fault slip inversions: Do they constrain stress or strain rate?, *J. Geophys. Res.*, *103*, 12,205–12,222.
Utsu, T. (1992), On seismicity, in *Report of the Joint Research Institute for Statistical Mathematics*, vol. 34, pp. 139–157, Inst. for Stat. Math., Tokyo.
Utsu, T. (1999), Representation and analysis of the earthquake size distribution: A historical review and some approaches, *Pure Appl. Geophys.*, *155*, 509–535.
Vavrycŭk, V. (2002), Non-double-couple earthquakes of 1997 January in West Bohemia, Czech Republic: Evidence of tensile faulting, *Geophs. J. Int.*, *149*, 364–373.
Vavrycŭk, V. (2005), Focal mechanisms in anisotropic media, *Geophs. J. Int.*, *161*, 334–346.
Vidale, J. (1988), Finite-difference calculation of traveltimes, *Bull. Seismol. Soc. Am.*, *78*, 2062–2076.
Waldhauser, F., and W. L. Ellsworth (2000), A double-difference earthquake location algorithm: Method and application to the Northern Hayward Fault, California, *Bull. Seismol. Soc. Am.*, *90*, 1353–1368.
Ward, P. L., G. Pálmason, and C. Drake (1969), Microearthquake survey and the Mid-Atlantic Ridge in Iceland, *J. Geophys. Res.*, *74*, 665–684.
Warren, N. W., and G. V. Latham (1970), An experimental study of thermally induced microfracturing and its relation to volcanic seismicity, *J. Geophys. Res.*, *75*, 4455–4464.
Wiemer, S., and S. McNutt (1997), Variations in frequency-magnitude distribution with depth in two volcanic areas: Mount St. Helens, Washington, and Mt. Spurr, Alaska, *Geophys. Res. Lett.*, *24*, 189–192.
Wiemer, S., and M. Wyss (2002), Mapping spatial variability of the frequency-magnitude distribution of earthquakes, *Adv. Geophys.*, *45*, 259–302.

Woessner, J., and S. Wiemer (2005), Assessing the quality of earthquake catalogues: Estimating the magnitude of completeness and its uncertainty, *Bull. Seismol. Soc. Am.*, *95*, 684–698.

Wyss, M. (1973), Towards a physical understanding of the earthquake frequency distribution, *Geophys. J. R. Astron. Soc.*, *31*, 341–359.

Wyss, M., and J. N. Brune (1968), Seismic moment, stress, and source dimensions for earthquakes in the California-Nevada region, *J. Geophys. Res.*, *73*, 4681–4694.

Wyss, M., B. Liang, W. R. Tanigawa, and X. Wu (1992), Comparison of orientations of stress and strain tensors based on fault plane solutions in Kaoiki, Hawaii, *J. Geophys. Res.*, *97*, 4769–4790.

Zierenberg, R. A., et al. (2012), Composition and origin of rhyolite melt intersected by drilling in the Krafla geothermal field, Iceland, *Contrib. Mineral. Petrol.*, *165*, 327–347.

Zoback, M. L., and M. Zoback (1980), State of stress in the conterminous United States, *J. Geophys. Res.*, *85*, 6113–6156.